Turbulent thermal convection in a finite domain: Part II. Numerical results

H. Park and L. Sirovich
Center for Fluid Mechanics and The Division of Applied Mathematics, Brown University, Providence, Rhode Island 02912

(Received 10 January 1990; accepted 8 May 1990)

A pseudospectral method is used to solve the Boussinesq equations for a fully inhomogeneous turbulent flow. The numerical data are analyzed using the empirical eigenfunction technique. As a result of the underlying inhomogeneity of the flow, the eigenfunctions (structures) are inhomogeneous in all three directions. This is the first instance in which fully three-dimensional empirical eigenfunctions have been calculated. The generated basis set is extremely efficient at depicting the flow. The first eigenfunction captures almost 60% of the average energy. The eigenfunctions are an optimal basis for capturing the energy of the flow and more than 95% of the energy is captured by the first 100 eigenfunctions. Ten classes of eigenfunctions are present and examples of each are shown. The average Nusselt number for the bounded geometry is found to be lower than that for a correspondong homogeneous case and the physics causing this decrease is analyzed and discussed.

I. INTRODUCTION

The Rayleigh–Bénard convection problem has been subject to a long history of numerial simulations.[1–7] In recent times large scale calculations have been performed for flows well into the chaotic regime.[5,8–11] The most tractable of these problems is the so-called slippery boundary value problem in which the heated surfaces are impermeable, stress-free, and the flow is horizontally unbounded.[12–14] This is the case treated in Ref. 5 and 8. The no-slip case that is more realistic from the perspective of experiment has been treated by Eidson *et al.*,[4] however, their fluid is also unconfined in the spanwise directions. A calculation in which the fluid is fully confined with no-slip boundary conditions has been discussed by Kessler.[15] But this has a number of limitations in terms of Rayleigh number and imposed symmetries on the solution.

Several investigations, in confined geometries, do exist for relatively low values of Ra. For example Toomre *et al.*[16,17] and Massaguer and Mercader[18] consider a hexagonal platform and Jones *et al.*[19] consider a cylindrical geometry. Unlike the present study, the aforementioned studies are aimed at stability and the transition to unsteady convection. As a result, low-order highly truncated modal systems are employed in these investigations. In these studies *swirl* (vertical vorticity) is found to play a role and, in particular, in Ref. 18, it is claimed that swirl enhances the rate of heat transfer. Likewise, in our investigation, the presence of horizontal confinement, produces classes of modes that produce swirl. However, we feel that the explanation given by Massaguer and Mercader for the enhanced heat transfer, in the confined geometry, is not relevant to our case. And in fact the heat transfer is less than it would be in the unbounded case.

The computation discussed in this paper applies to fully confined R–B convection problem. In addition to adding our general body of knowledge on R–B convection, this problem has a number of features that deserve consideration. As mentioned, we are interested in chaotic convection. For such flows the unbounded cases mentioned above are statistically homogeneous in the spanwise directions. The present calculation, by contrast, is inhomogeneous in all three directions. As a result ensemble-averaged quantities now show inhomogeneities in all directions. In particular, quantities such as heat flow and rms fluctuations show interesting variations across a planform.

Our principal method of analyzing the resulting flow is by means of the Karhunen–Loève (K–L) procedure[20] introduced by Lumley[21–23] for the extraction of *coherent structures.* As is well known the resulting *structures* are pure sinusoids in any homogeneous direction[22,24] and this has led to techniques for reassembling the *structures* so as to make them compact.[23] Thus an important property of the structures that emerge here is that they are immediately compact as a result of the underlying inhomogeneity of the flow and no additional assumptions are required.

An interesting, and perhaps counterintuitive, consequence of our simulation is the fact, mentioned above, that the heat transfer rate is less than it would be in the spanwise unbounded case under the same conditions. For, in the latter case, pure horizontal motions take place that in no way contribute to the transport of heat. Owing to impermeable side walls such motions are not possible in the case treated here. The motion is forced into the vertical direction which would appear to facilitate heat transfer. To resolve this seeming paradoxical result we can turn to the Malkus theory[25] and its extension by Spiegel.[26] In those theories the heat transfer is shown to increase with Ra due to the excitation of an increasing number of modes. In the Malkus theory it is the linear stability eigenfunctions, while in the Spiegel theory it is the *mean field* eigenfunctions that are considered. The empirical eigenfunctions developed here are the natural extension of the linear and mean field eigenfunctions in such highly nonlinear situations as considered here. It will be seen in Sec. V, at comparable Ra, that fewer empirical eigenfunctions are excited in the restricted geometry compared with the unrestricted geometry, thus accounting for the decreased heat flow.

 0899-8213/90/091659-10$02.00

II. NUMERICAL PROCEDURES

The Boussinesq equations and boundary conditions for the present investigation are to be found in Ref. 27 [henceforth referred to as (I)], and for convenience are repeated here in a slightly different form

$$\nabla\cdot\mathbf{u}=0, \tag{1}$$

$$\frac{\partial\mathbf{u}}{\partial t}-\mathbf{u}\wedge\boldsymbol{\omega}=-\nabla(p+u^2/2)+\mathrm{Ra}\,\mathrm{Pr}\,\mathbf{e}_z T+\mathrm{Pr}\nabla^2\mathbf{u}. \tag{2}$$

$$\frac{\partial T}{\partial t}+\mathbf{u}\cdot\nabla T=w+\nabla^2 T, \tag{3}$$

where $\boldsymbol{\omega}$ is vorticity, and

$$\begin{aligned} &w=T=\frac{\partial u}{\partial z}=\frac{\partial v}{\partial z}=0 \quad \text{at } z=0,1,\\ &u=\frac{\partial T}{\partial x}=\frac{\partial v}{\partial x}=\frac{\partial w}{\partial x}=0 \quad \text{at } x=0,2,\\ &v=\frac{\partial T}{\partial y}=\frac{\partial u}{\partial y}=\frac{\partial w}{\partial y}=0 \quad \text{at } y=0,2. \end{aligned} \tag{4}$$

Equations (4) specify (slip) stressless conditions at all boundaries, adiabatic side walls, and specified temperatures at the upper and lower boundaries. The aspect ratio of 2 includes the most dangerous mode from linearized stability theory and the square planform leads to maximal data extension (I).

A pseudospectral method[28] is employed. Thus, to meet the boundary conditions (4) we approximate w, for example, by

$$w\approx\sum_{0\leqslant k,l,m\leqslant M}\hat{w}(k,l,m)\cos\frac{\pi kx}{2}\cos\frac{\pi ly}{2}\sin\pi mz, \tag{5}$$

where M is sufficiently large to resolve all relevant scales (discussed later). It is clear from (3) that T takes on the same series form as (5) while u and v are developed with appropriate permutations of the trigonometric functions. The gradient term in (2) can be eliminated by means of the incompressibility condition (1) and the result of this and substitution of (5) yields,

$$\frac{d}{dt}\hat{\mathbf{u}}+\mathrm{Pr}\,k^2\hat{\mathbf{u}}=\frac{1}{k^2}\mathbf{k}\wedge\widehat{(\mathbf{u}\wedge\boldsymbol{\omega})}-\frac{\mathrm{Ra}}{k^2}\mathrm{Pr}\,\hat{T}\mathbf{k}\wedge(\mathbf{k}\wedge\mathbf{e}_z), \tag{6}$$

$$\frac{d}{dt}\hat{T}+k^2\hat{T}=-i\mathbf{k}\cdot\widehat{(\mathbf{u}T)}+\hat{w}. \tag{7}$$

As in (5) the caret denotes Fourier transformation. As is customary in the pseudospectral method, products are evaluated in physical space and derivatives in Fourier space, since the fast Fourier algorithm allows rapid passage between the spaces.

To indicate the method of integration we express (6) and (7) symbolically as

$$\frac{d\mathbf{X}}{dt}+\mathbf{A}\mathbf{X}=\mathbf{B}(\mathbf{X}), \tag{8}$$

where $\mathbf{X}=(\hat{\mathbf{u}},\hat{T})$. This can be formally integrated to give

$$\mathbf{X}(t+\Delta t)=e^{-2\mathbf{A}\Delta t}\mathbf{X}(t-\Delta t)+\int_{t-\Delta t}^{t+\Delta t}e^{-\mathbf{A}(t+\Delta t-\tau)}\mathbf{B}(\tau)d\tau. \tag{9}$$

We use a time marching scheme based on a leapfrog for the nonlinear terms and an exact integration for the linear part.[28] After applying the leapfrog scheme to the integral in (9), the expression for the time-stepping scheme is obtained,

$$\mathbf{X}(t+\Delta t)=e^{-\mathbf{A}2\Delta t}\mathbf{X}(t-\Delta t)+2\Delta t e^{-\mathbf{A}\Delta t}\mathbf{B}(t). \tag{10}$$

The leapfrog scheme is known to be slightly unstable. To compensate for this, we use a second-order Runge–Kutta scheme at every $2M$ time steps. As initial conditions, we adopt a velocity field of an independent, Gaussian distributed random variable with isotropic energy density distribution.

The time step of integration was $\Delta t=0.001$, in the dimensionless units of (1–3). The ratio of the Kolmogorov time scale, $(\nu/\epsilon)^{1/2}$ to Δt is 28.3 (ϵ is the average value of turbulence dissipation). The dimensionless Kolmogorov microscale was 0.0404 based on $\eta=(\nu^3/\epsilon)^{1/4}/H$. Questions of spatial resolution have been addressed by Grotzbach[29] who determined that the maximum resolvable wave number should exceed $1/\eta$. If h denotes the vertical grid spacing, the condition is

$$\pi\eta H/h>1. \tag{11}$$

In the present simulation this ratio had the value 2.03. Thus both the spatial and temporal scales have been resolved.

Another test of the spatial resolution can be based on the Nusselt number

$$\mathrm{Nu}=H/2\delta, \tag{12}$$

where δ is a measure of the (linear) thermal sublayer. In this view δ is the smallest scale of the problem. As we will see the maximum value of Nu is 6, and since the calculation contains 16 uniform grid spacings in all directions, the problem is also resolved from this point of view.

Since the grid system, $(17)^3$, might be regarded as marginal we also perform the calculation on a $(33)^3$ grid. This resulted in no significant changes in the solution.

III. RESULTS

The numerical calculation was carried out at $\mathrm{Pr}=0.72$ and at a Rayleigh number of

$$\mathrm{Ra}\approx 70\mathrm{Ra}_c\approx 46\,000, \tag{13}$$

where the critical Rayleigh number is

$$\mathrm{Ra}_c=27\pi^4/4\approx 657. \tag{14}$$

The grid system was taken to be $(17)^3$, i.e., $M=17$ in (5). Thus $(17)^3\times 4\approx 2\times 10^4$ field quantities are saved at each time step.

Table I contains a summary of statistical results for the present simulation. For purposes of comparison we also list the results obtained in a simulation at the same Pr and Ra, for a flow that is unbounded in the horizontal directions.[9]

All quantities have been averaged in the midplane. Viewing the quantities presented we see that the flow is mildly chaotic. It is more vigorous than the comparable horizontally unbounded flow. But in spite of this the Nusselt number is somewhat smaller, indicating that the side walls do not aid heat transport. It is interesting to observe that Re_{λ_u}, the horizontal skewness, and the horizontal flatness are all significantly larger than the unbounded case. This is also in keep-

TABLE I. Comparison of significant statistical averaged. All calculations are for $Ra = 70Ra_c$ and are midplane averaged.

	Unbounded	Bounded
$\lambda_u = \left(\frac{\langle u^2\rangle}{\langle(\partial u/\partial x)^2\rangle}\right)^{1/2}$	0.29	0.324
$Re_{\lambda_u} = \langle u^2\rangle^{1/2}\lambda_u/\nu$	12.60	14.93
$\left\langle\left(\frac{\partial u}{\partial x}\right)^3\right\rangle\left\langle\left(\frac{\partial u}{\partial x}\right)^2\right\rangle^{-3/2}$	−0.15	−0.2420
$\left\langle\left(\frac{\partial u}{\partial x}\right)^4\right\rangle\left\langle\left(\frac{\partial u}{\partial x}\right)^2\right\rangle^{-2}$	3.76	4.60
$\lambda_w = \left[\langle w^2\rangle\left\langle\left(\frac{\partial w}{\partial z}\right)^2\right\rangle^{-1}\right]^{1/2}$	0.49	0.663
$Re_{\lambda_w} = \langle w^2\rangle^{1/2}\lambda_w/\nu$	38.1	40.27
$\left\langle\left(\frac{\partial w}{\partial z}\right)^3\right\rangle\left\langle\left(\frac{\partial w}{\partial z}\right)^2\right\rangle^{-3/2}$	−0.65	−0.42
$\left\langle\left(\frac{\partial w}{\partial z}\right)^4\right\rangle\left\langle\left(\frac{\partial w}{\partial z}\right)^2\right\rangle^{-2}$	4.85	4.415
Nusselt number	5.9	5.75
Prandtl number	0.72	0.72

ing with the more vigorous nature of the present flow over the unbounded case. On the other hand, the vertical counterparts in the two cases are more comparable.

Since the flow is inhomogeneous in all three directions, ensemble-averaged quantities vary with x and y as well as z. As an illustration of this point we show in Fig. 1 the ensemble-averaged Nusselt number as a function of position on a horizontal boundary, $z = 0,1$. It is clearly inhomogeneous, with the symmetry of Fig. 1 being due to the group averaging procedure, see (I). [In (I), Fig. 3, we show $\langle T\rangle$ at several (x,y) locations that further underlines this inhomogeneity.]

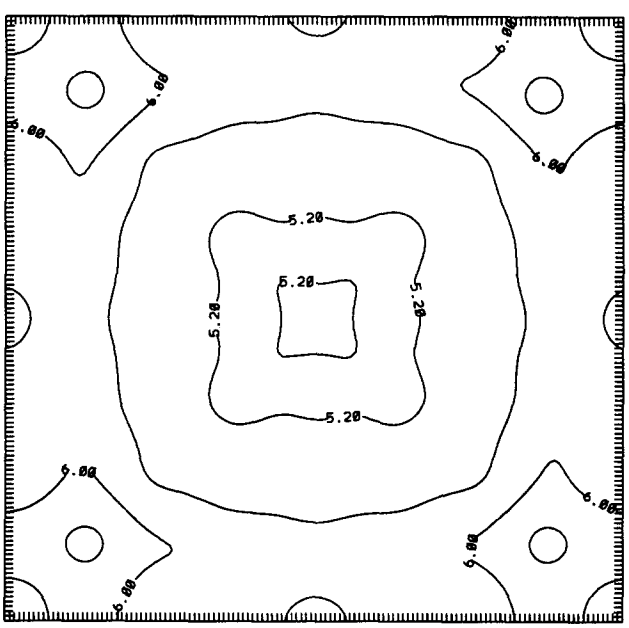

FIG. 1. The ensemble-averaged Nusselt number as a function of position on a vertical boundary, $z = 0,1$.

Figure 2 shows the average mean temperature, $\overline{T}$, and the averaged mean-square vertical velocity, $\overline{w^2}$ (indicated by continuous curves). This is compared with the results of the calculation at the same ratio of Ra/Ra_c, but with periodic boundary conditions.[9] In Fig. 3 we show the variation of mean-square vertical velocity with position. The continuous curve, which shows the largest variation, depicts conditions in a corner, where all the motion is vertical. Significant variation in the curves is seen to occur as we pass from the corner to the center. Unlike the horizontally homogeneous case, the present calculation leads to a nonzero mean flow, $\langle \mathbf{u}\rangle \neq 0$. This was illustrated in [(I): Fig. 2)], and is again discussed in the next section.

The matrix, $K_{ij}(\mathbf{x},\mathbf{x}')$, is fully inhomogeneous and therefore a function of six independent variables. In order to view some features of the $\mathbf{K}$ we averge over horizontal planes as follows:

$$\hat{\mathbf{K}}(z,z') = \int dx\, dy\, \mathbf{K}(x,y,z,x,y,z'). \tag{15}$$

In Fig. 4 we show

$$\begin{aligned}\langle \hat{w}(z)\hat{w}(z')\rangle &= \hat{K}_{33},\\ \langle \hat{w}(z)\hat{\theta}(z')\rangle &= \hat{K}_{34},\end{aligned} \tag{16}$$

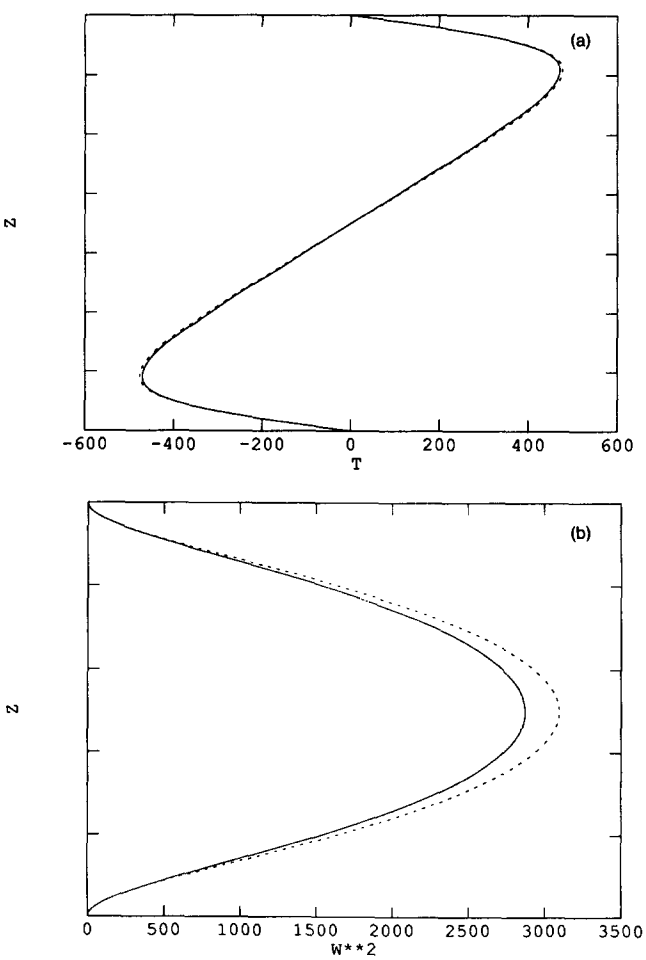

FIG. 2. (a) and (b) The mean temperature and the mean-square vertical velocity indicated by continuous curves. This is compared with the results with periodic boundary conditions (dashed lines).

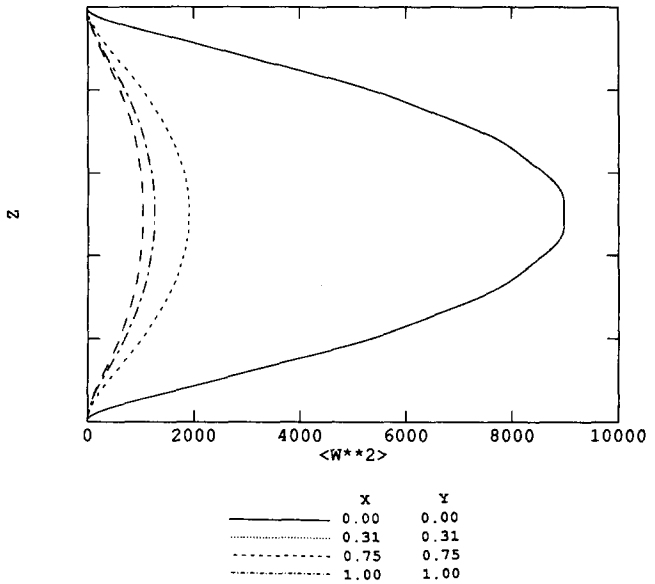

FIG. 3. Vertical velocity variation at several (x,y) locations.

where a circumflex on the left-hand side indicates the variables being considered. The variation of these quantities is directly related to already computed quantites. For example, $\hat{K}_{33}(z,z) = \overline{w^2}$, so that the variation of $\hat{K}_{33}$ across the diagonal is the same as the vertical variation of w^2. The variation of $\hat{K}_{34}$ across the diagonal,

$$\hat{K}_{34}(z,z) = \overline{w\theta}, \tag{17}$$

is the turbulent heat transport. (We discuss $\overline{w\theta}$ in Sec. V.) As is well known $\overline{w\theta}$ vanishes at the boundary and is well approximated by a constant in the core. All of this is borne out in Fig. 4(b). Of additional interest is the fact that the peak correlation occurs off the diagonal! The peak correlation, which is almost 50% above the core value of $\overline{w\theta}$, appears when $z \approx \frac{1}{2}$ and z' is near the edge of the thermal boundary. As is clear from Fig. 2(b) the vertical velocity peaks at the centerplane. On the other hand, thermal fluctuations peak at the edge of the thermal boundary layer. As we will see in the next section, the dominant mode of motion is a single roll. Thus, although not perfectly correlated, there is a substantial degree of correlation between the boundary layer and the midsection that is forced by the rolling motion. This is especially true near the side walls, where the vertical velocity w peaks (see Fig. 3). Therefore the peaks in Fig. 4(b) are due to a combination of coherence in the motion and the large values of θ_{rms} and w_{rms}.

IV. EIGENFUNCTION ANALYSIS

While it is useful and informative to consider the averaged quantities discussed in the previous section, a deeper understanding follows when the flow is resolved in terms of the empirical eigenfunctions, (I). We recall from (I) that to obtain these we first construct the two-point correlation

$$K_{mn}(\mathbf{x},\mathbf{x}') = \langle v_m(\mathbf{x}) v_n(\mathbf{x}') \rangle, \tag{18}$$

where

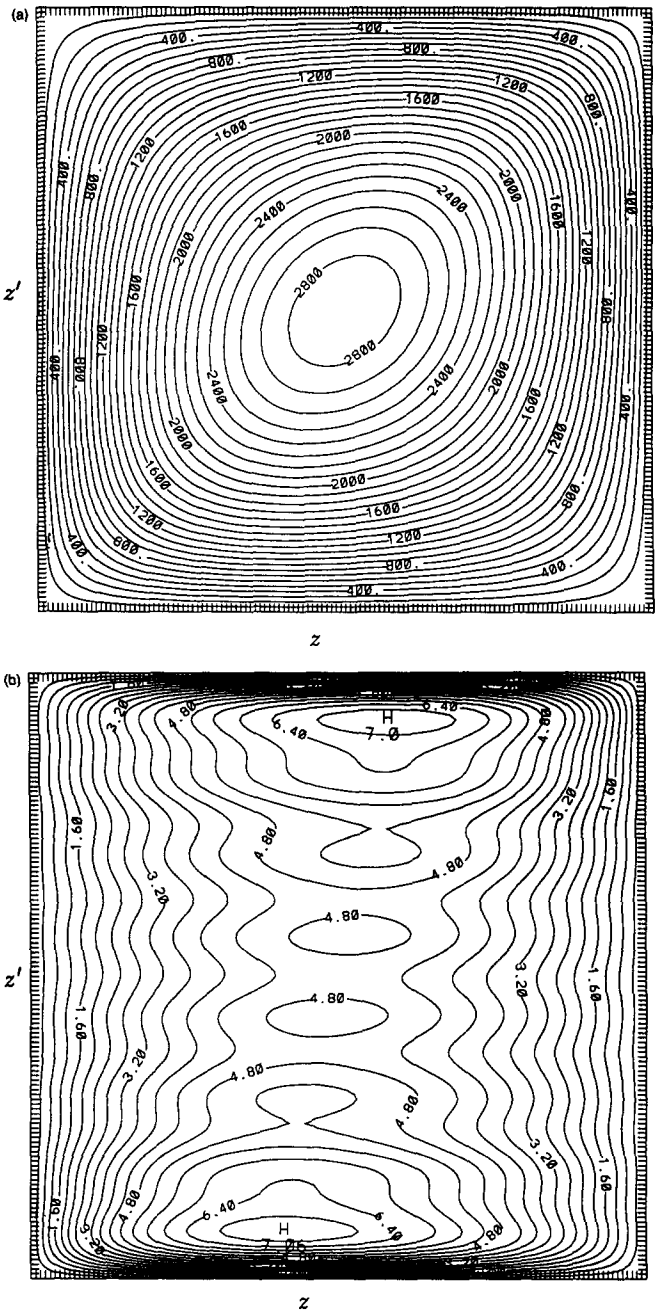

FIG. 4 Level lines of the averaged two point correlation. (a) $\langle \hat{w}(z)\hat{w}(z') \rangle$, (b) $\langle \hat{w}(z)\hat{\theta}(z') \rangle$.

$$\mathbf{v} = (\mathbf{u},\theta) \tag{19}$$

is the fluctuating flow and then consider the eigenfunction equation

$$\int_V \mathbf{K}(\mathbf{x},\mathbf{x}')\phi(\mathbf{x}')d\mathbf{x}' = \lambda\phi(\mathbf{x}), \tag{20}$$

where integration is over the domain of the flow, V.

The eigenvalues are listed in Table II in descending order. We recall that an eigenvalue represents the mean energy of the system projected onto the corresponding eigenspace. The eigenfunctions can be split into ten symmetry classes. These can be put in correspondence with the ten projectors

TABLE II. Empirical eigenvalues. All members of $E_1^{\pm}$ are doubly degenerate and no other generic degeneracy.

Number	Projector	Quantum number	Eigenvalue	% total energy
1	E_1^-	1	0.5996	59.96
2	E_1^+	1	0.1306	13.06
3	E_5^-	1	0.0266	2.66
4	E_1^+	2	0.018	1.8
5	E_3^+	1	0.017 67	1.767
6	E_2^-	1	0.013 71	1.371
7	E_1^-	2	0.014	1.4
8	E_2^+	1	0.0127	1.27
9	E_4^+	1	0.008	0.8
10	E_4^-	1	0.007	0.7

$E_p^{\pm}, p = 1,...,5$. *Thus the second column lists the symmetry class. All members of* $E_1^{\pm}$ are doubly degenerate, while the remaining eigenfunctions show no generic degeneracy. The third column lists the ranking or quantum number within a class, the fourth the normalized value of eigenvalue, and fifth the percent of the total energy.

Thus we see that almost 60% of the energy of the flow is captured by the invariant subspace associated with the first eigenfunction. Figure 5 plots the variation of energy capture versus the number of eigenfunctions (degeneracy included). Thus more than 90% of the energy is captured by the first 40 eigenfunctions and more than 95% by the first 100 eigenfunctions.

Figure 6 along with Figs. 2 and 5 in (I) depict representative eigenfunctions for each of the ten symmetry classes. To generate a second member of the invariant subspace corresponding to any $E_1^{\pm}$ symmetry class the flow is rotated by $\pi/2$ about the vertical axis. This specifically applies to Fig. 5 in (I) and to Fig. 6(f). Each of the eigenfunctions also carry a temperature variation. Two of these are depicted in Fig. 7. Figure 7(a) is the temperature variation associated with E_1^- and therefore goes with Fig. 5 of (I), and Fig. 7(b) is associated with E_5^+ and goes with Fig. 2 of (I).

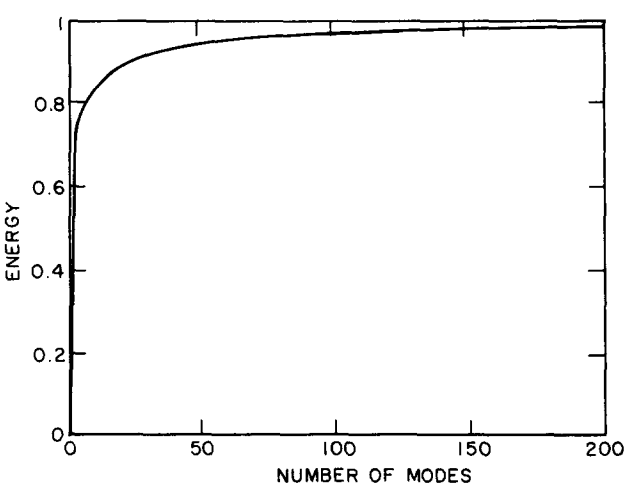

FIG. 5. The variation of energy captured versus the number of eigenfunctions (degeneracy included).

As a check on the convergence of the numerical simulation we can monitor the variation of the eigenvalues as the number of snapshots is varied. This is shown for the first four eigenfunctions in Fig. 8. We see from this that these appear to have reached their asymptotic values. The corresponding eigenfunctions themselves, converge much more rapidly.

V. DISCUSSION

Although the flow in the convection cell is statistically steady there are sharp temporal variations. This is illustrated by the temporal variation of averged values of Nu and Re_{λ_w} shown in Fig. 9 due to the sampling. (The curves shown represent sampling times taken at every 600 time steps. As mentioned earlier, the temporal evolution is well resolved although it might not appear so from Fig. 9.) It might be felt that this does not represent a sufficient long record, however, one should bear in mind that as a result of the symmetry variations represented in (I) the record is effectively 16 times as long.[27] The sharp changes in the net heat flow at the boundaries are due to changes in the convective patterns at the *walls.* This as well as the other features are well brought out by analyzing the simulation in terms of the empirical eigenfunctions. Specifically if $\mathbf{v}$ denotes the flow fluctuation, (19), then we may write

$$\mathbf{v} = \sum_n a_n(t)\phi^{(n)}(\mathbf{x}), \tag{21}$$

where $\{\phi_n\}$ are the orthonormal eigenfunctions of (20), and

$$a_n(t) = \int_V (\phi^{(n)}(\mathbf{x}), \mathbf{v}(\mathbf{x},t))d\mathbf{x}. \tag{22}$$

Thus the simulation may be reexpressed in the form (21) by generating the time series for $a_n(t)$ with the use of (22). As is immediate,

$$\langle a_n a_m \rangle = \lambda_n \delta_{nm}, \tag{23}$$

supporting the usage of *average energy* (in the $\phi^{(n)}$ mode) for λ_n.

As an indication of the convergence of the empirical eigenfunctions we consider the variation of

$$\mathbf{v}_N = \sum_{n=1}^{N} a_n(t)\phi^{(n)}(x)$$

with N. Figure 10 indicates graphically this convergence in terms of the vertical velocity.

Since most of the energy resides in the first eigenfunction shown in Fig. 5 of (I) we consider this first. Note that this depicts a *roll,* the streamlines of which do not lie in (x,z) planes, but are somewhat warped. A second eigenfunction in the same invariant subspace is obtained by rotating by $\pi/2$ about the vertical axis. Thus any admixture of these two eigenfunctions is also an eigenfunction.

Figure 11 shows the time series in terms of amplitude and orientation of the roll. The horizontal line in Fig. 11(a) indicates the eigenvalue λ_1, which is also the average of the corresponding *rolling* energy in this mode. As Fig. 11(b) shows, the roll is initially oriented along the x axis and oscillates around the zero angle. At roughly $t = 160$ the roll rotates by $\pi/2$ and is oriented along the y axis. Near the end of

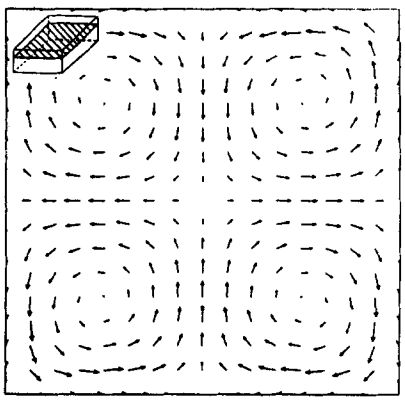

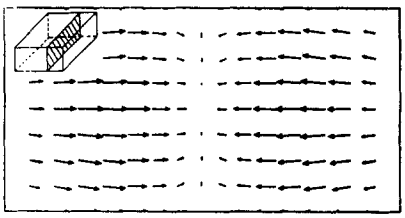

E_2^+

(a)

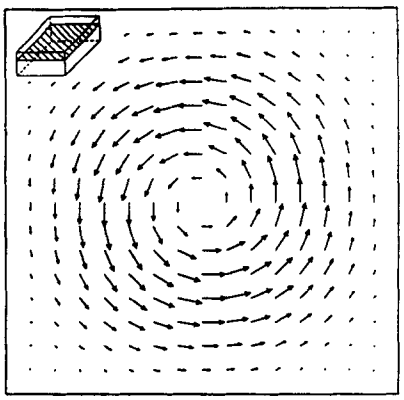

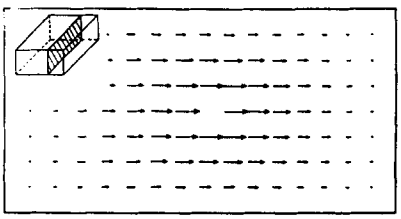

E_3^+

(b)

FIG. 6. (a)–(h) Principal eigenfunctions for projected eigensubspaces as indicated. Inserts indicate planes in which flow lines are shown.

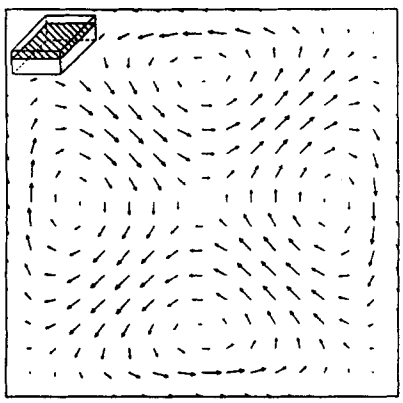

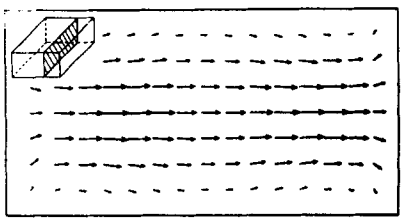

E_4^+

(c)

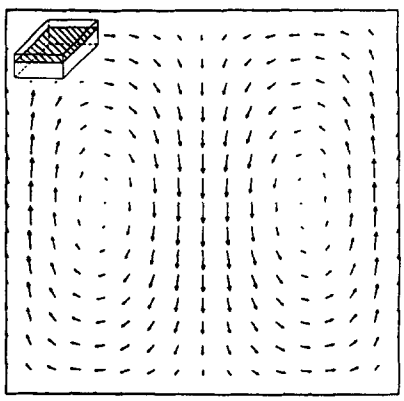

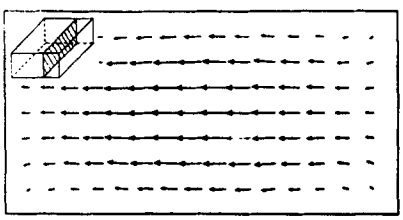

E_1^+

(d)

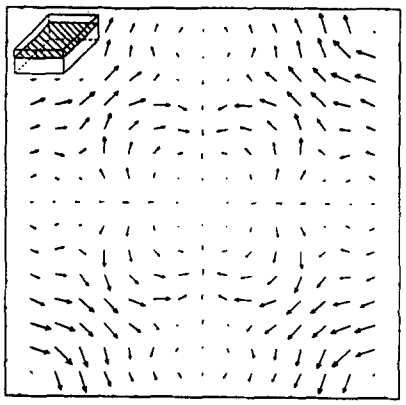

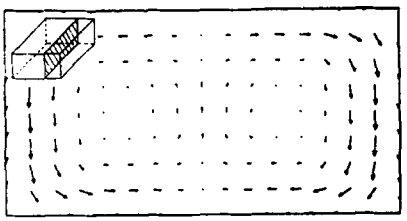

E_2^-

(e)

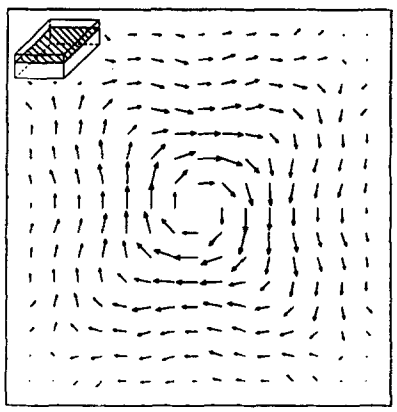

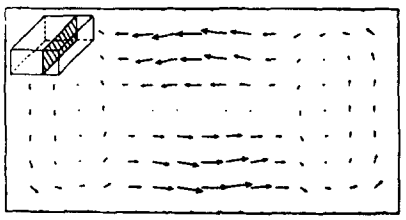

E_3^-

(f)

FIG. 6. (Continued.)

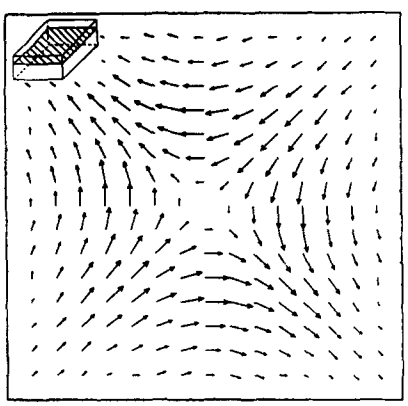

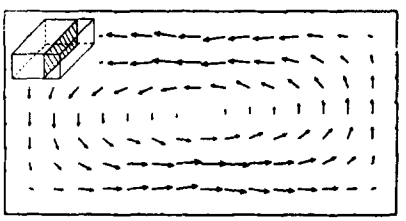

E_4^-

(g)

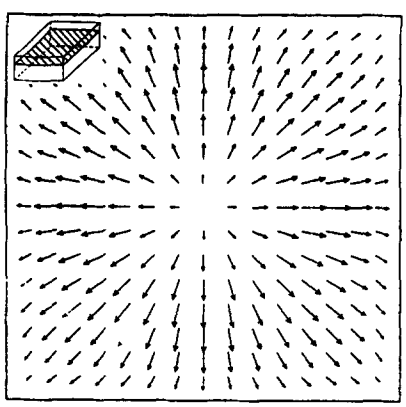

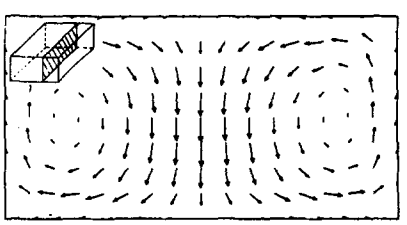

E_5^-

(h)

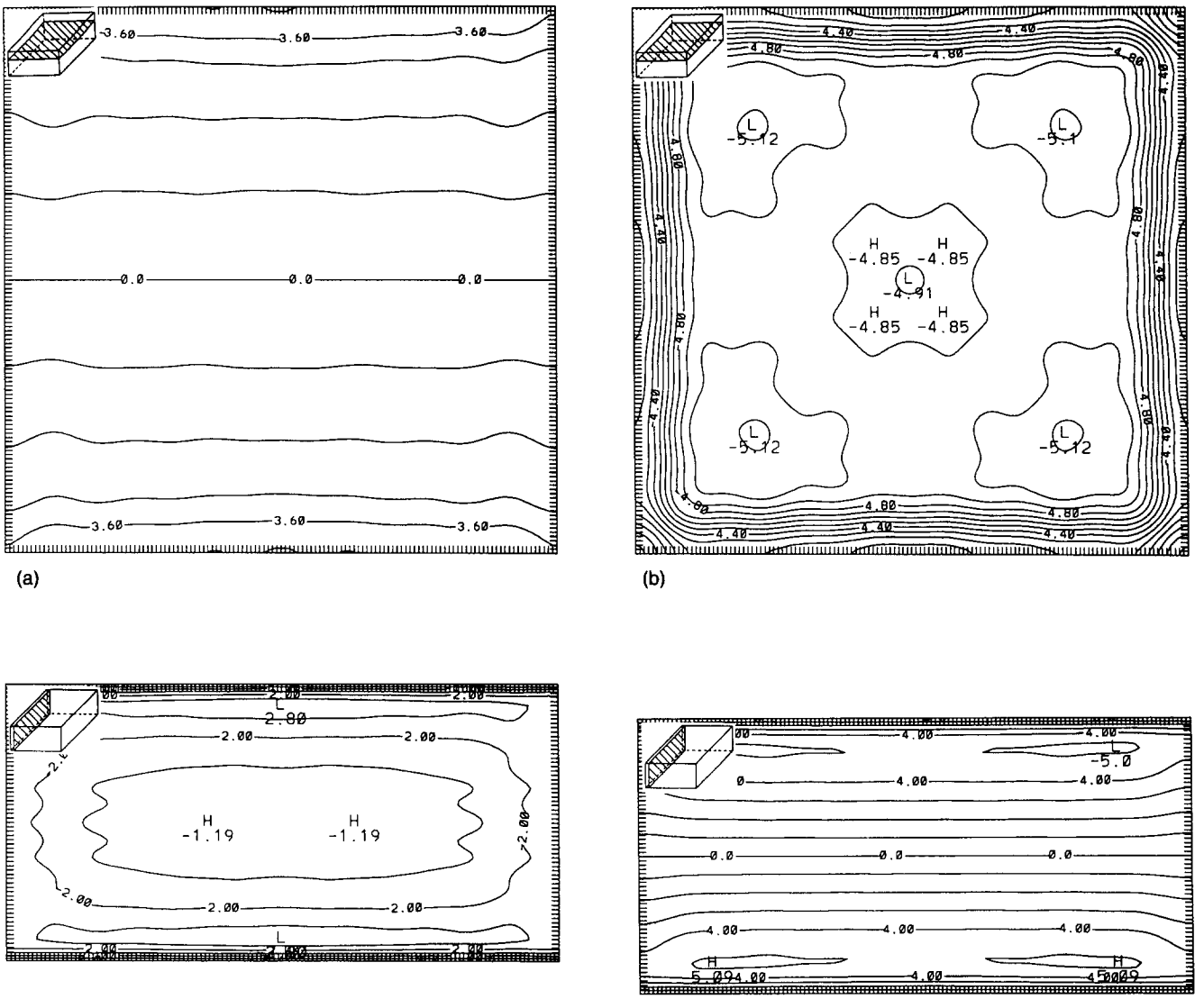

FIG. 7 (a) The principal temperature eigenfunction for the projected subspace E_1^-. (b) The principal temperature eigenfunction for the projected subspace E_5^+.

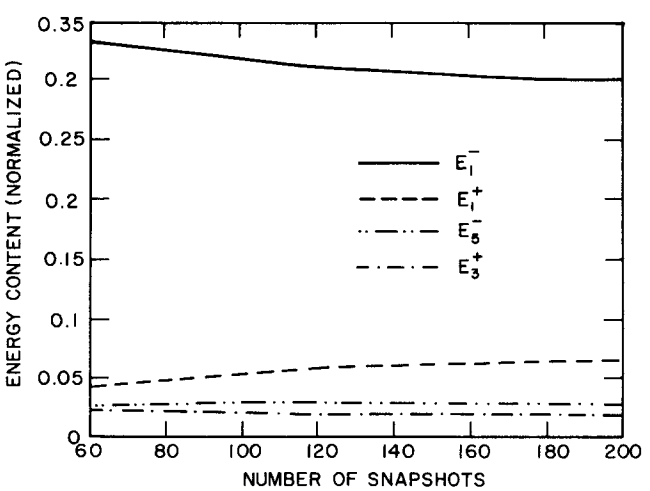

FIG. 8. The variation of eigenvalues as the number of snapshots.

the simulation this rotates once again by $\pi/2$ so that it is again aligned on the x axis but not counter-rotating relative to the initial rotation.

In light of the correction by Siggia and Zippelius[30] to the Newell and Whitehead equation[31] due to vertical vorticity it is of interest to see what role this vorticity plays here. An examination of the eigenfunctions in Figs. 6(b) and 6(f) shows that these possess significant vertical vorticity or swirl. (Other modes also carry some swirl.) It is worth pointing out that these are *parasitic* modes in the sense that the motion, which is horizontal, is perpendicular to the vertical driving force. By contrast, for the unbounded convection calculation,[9] the counterparts to these modes are horizontal shearing modes, and therefore have their vorticity in the horizontal. The vertical boundaries inhibit spanwise motion and therefore cause the swirl. There are significantly more ways in which to generate swirl in the present case.

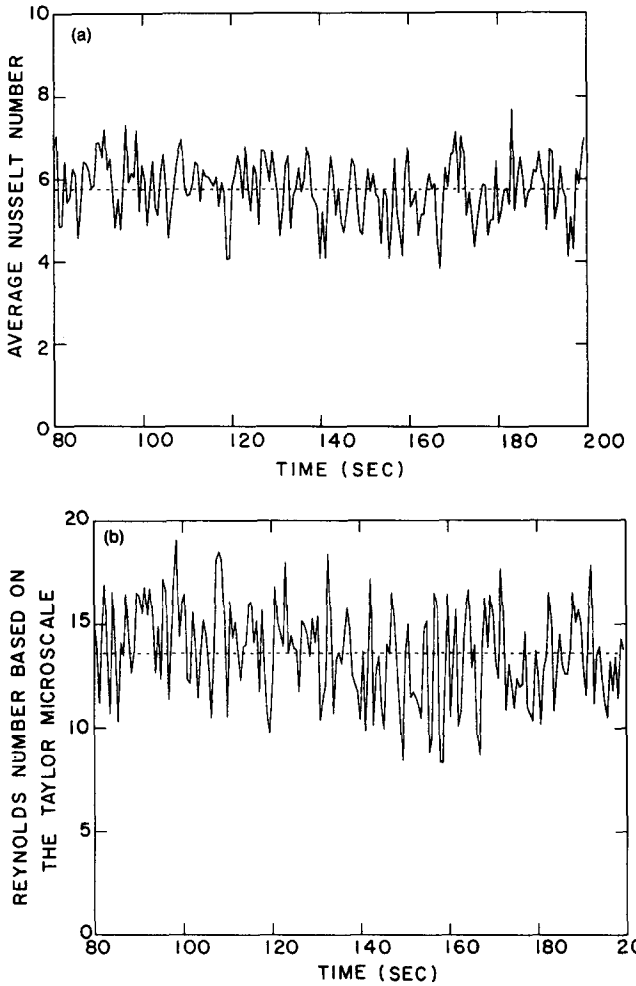

FIG. 9 (a) The temporal variation of averaged Nusselt number. (b) The temporal variation of averaged Reynolds number based on the Taylor microscale.

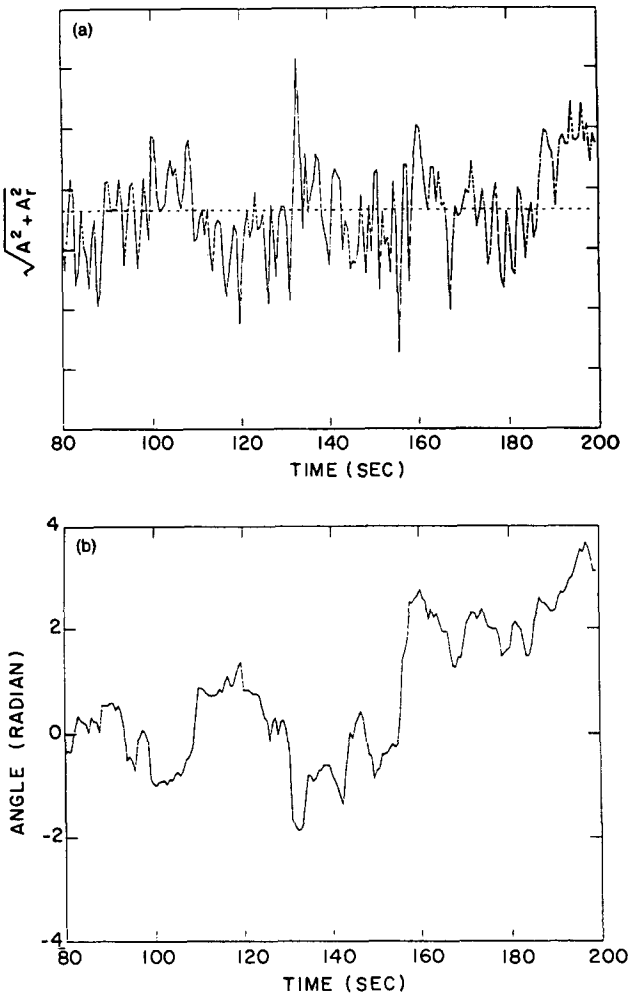

FIG. 11. (a) and (b) The time series for the coefficients [Eq. (22)] of the first two (degenerated) eigenfunctions from the subspace E_1^- in terms of amplitude $\left[\sqrt{a_r^2(t) + a_i^2(t)}\right]$, and phase $(\tan^{-1}[a_r(t)/a(t)])$.

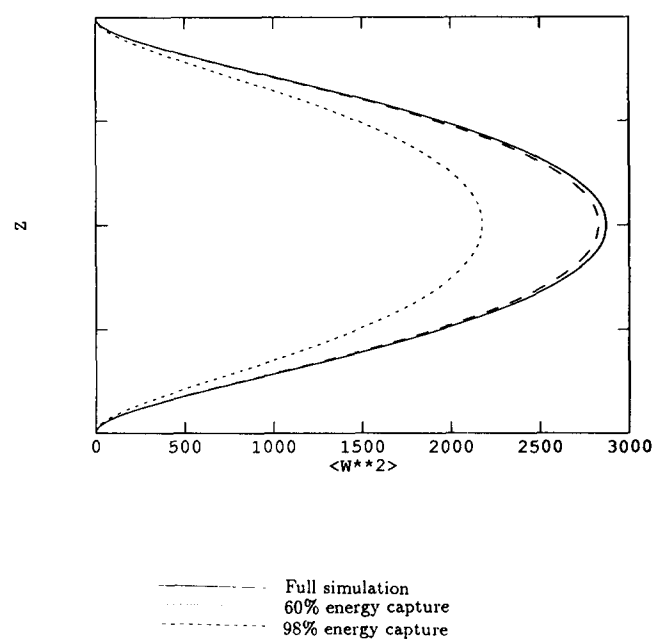

FIG. 10. Approximation by truncated series of eigenfunctions of the vertical velocity.

As mentioned earlier the Nusselt number is 5.75 for the present calculation. For the unbounded case,[9] at the same value of Ra, Nu $\approx$ 5.9. Thus the confined geometry produces a decrease in heat transport for a fixed Ra/Ra_c. At lower Ra an increase in heat transport, in a confined geometry (hexagonal cells), was noted by Massaguer and Mercader[18] and they attributed this to the appearance of swirl. Their argument, in essence, is that the nonlinear interaction of a swirling mode with modes carrying vertical velocity leads to enhanced heat transport. While the argument may appear plausible we now show that within the present framework this is not true.

If the energy equation is both ensemble averaged and averaged over the square planform we obtain

$$\overline{w\theta} = \frac{d\overline{T}}{dz} - \frac{d\,\overline{T_0}}{dz} \tag{24}$$

[see (I), Eq. (23)], where the constant term is the planform averaged temperature at a wall. In the main body of the flow the gradient term is negligible and we obtain

$$\frac{d\,\overline{T_0}}{dz} \approx -\,\overline{w\theta}. \tag{25}$$

To examine the form of the averaged turbulent convection, $\overline{w\theta}$, we express a typical eigenfunction as

$$\boldsymbol{\phi}^{(n)} = (\phi_1^{(n)}, \phi_2^{(n)}, \phi_3^{(n)}, \phi_4^{(n)}). \tag{26}$$

It then follows from the expansion (21) and the statistical orthogonality (23) that

$$\langle w\theta \rangle = \sum_n \lambda_n \phi_3^{(n)}(\mathbf{x}) \phi_4^{(n)}(\mathbf{x}). \tag{27}$$

The main point is that (27) states that the turbulent heat transport is equal to the sum of the individual contributions from the eigenmodes—*without cross-talk.* On averaging over the x-y plane we remove the x-y dependence to obtain $\overline{w\theta}$. The swirling modes that contain negligible vertical velocity are insignificant. Interaction of the sort described by Massaguer and Mercader[18] can lead to temporal fluctuations in heat transport but cannot contribute to the averaged value of this quantity.

As described in the Introduction, for the present calculation the diminished heat transport, due to the more restrictive boundary condition, is caused by fewer active modes at comparable Ra. The theory of Malkus[25] as well as his experiments[32] indicate that the heat flux increases in *discrete transitions* in a manner related to the appearance of unstable modes. The counterpart to this idea, in the present framework, is the degree of excitation of the modes, as seen in Table II. Compared to the unbounded study at the same Ra[8,9] relatively few modes reach a criterion level of energy in the present instance. This acts to lower the net heat flux. A compensating factor is the fact that, unlike the unbounded case, no mode is now without a vertical velocity component. Perhaps this accounts for Nu not being even lower than it is.

ACKNOWLEDGMENTS

Computations were performed on the Cyber 205 Supercomputer at the John von Neumann National Computer Center.

This work here was supported by DARPA-URI N00014-86-K0754.

[1] F. H. Busse and R. M. Clever, J. Fluid Mech. **91**, 319 (1979).
[2] F. H. Busse and J. A. Whitehead, J. Fluid Mech. **47**, 305 (1971).
[3] F. H. Busse, in *Instability of Continuous Systems,* edited by H. Leipholz (Springer, Berlin, 1971), pp. 41–17.
[4] T. M. Eidson, M. Y. Hussaini, and T. A. Zang, ICASE Report No. 86-6, 1986.
[5] J. H. Herring and J. Wyngaard, in *Fifth Symposium on Turbulent Shear Flows* (Springer, Berlin, 1986), pp. 10:39–10:43.
[6] J. B. McLaughlin and S. A. Orszag, J. Fluid Mech. **122**, 123 (1982).
[7] P. L. Sulem, C. Sulem, and O. Thual, Prog. Astronaut Aeronaut. **100**, 125 (1985).
[8] L. Sirovich, M. Maxey, and H. Tarman, in Sixth Symposium on Turbulent Shear Flow, Toulouse, France, 1987.
[9] L. Sirovich, H. Tarman, and M. Maxey, in *An Eigenfunction Analysis of Turbulent Thermal Convection,* edited by B. E. Launder (Springer, Berlin, 1988).
[10] L. Sirovich, S. Balachandar, and M. Maxey, Phys. Fluids A **1**, 1911 (1989).
[11] S. Balachandar, M. Maxey, and L. Sirovich, J. Sci. Comput. **4**(2), 219 (1989).
[12] P. G. Drazin and W. H. Reid, *Hydrodynamic Stability* (Cambridge U.P., London, 1981).
[13] S. Chandrasekhar, *Hydrodynamic and Hydromagnetic Stability* (Oxford U.P., London, 1961).
[14] F. H. Busse, Rep. Prog. Phys. **41**, 1929 (1978).
[15] R. Kessler, J. Fluid Mech. **174**, 357 (1987).
[16] J. Toomre, D. O. Gough, and E. A. Spiegel, J. Fluid Mech. **79**, 1 (1977).
[17] J. Toomre, D. O. Gough, and E. A. Spiegel, J. Fluid Mech. **125**, 90 (1982).
[18] J. M. Massaguer and I. Mercader, J. Fluid Mech. **189**, 367 (1988).
[19] C. A. Jones, D. R. More, and N. O. Weiss, J. Fluid Mech. **73**, 353 (1976).
[20] R. B. Ash and M. F. Gardner, *Topics in Stochastic Processes* (Academic, New York, 1975).
[21] J. L. Lumley, *Atmospheric Turbulence and Radio Wave Progagation,* edited by A. M. Yaglom and V. I. Tatarski (Nauka, Moskow, 1967), pp. 166–178.
[22] J. L. Lumley, *Stochastic Tools in Turbulence* (Academic, New York, 1970).
[23] J. L. Lumley, in *Transition and Turbulence,* edited by R. E. Meyer (Academic, New York, 1981), pp. 215–242.
[24] L. Sirovich, Q. Appl. Math. **XLV**(3), 561, 573 (1987).
[25] W. V. R. Malkus, Proc. R. Soc. London, Ser. A **225**, 185 (1954).
[26] E. A. Spiegel, Mècanique de la Turbulence, Centre Natl Rech. Sci. Paris, 181 (1962).
[27] L. Sirovich and H. Park, Phys. Fluids A **2**, 1649 (1990).
[28] C. Canuto, M. Y. Hussaini, A. Quarderonic, and T. A. Zang, *Spectral Methods in Fluid Dynamics* (Springer, New York, 1988).
[29] G. Grötzbach, J. Comput. Phys. **491**, 241 (1983).
[30] E. Siggia and A. Zippelius, Phys. Fluids **26**, 2905 (1983).
[31] A. C. Newell and J. A. Whitehead, J. Fluid Mech. **38**, 279 (1969).
[32] W. V. R. Malkus, Proc. R. Soc. London Ser. A **225**, 196 (1954).